Far-forward production of charm mesons and neutrinos at forward physics facilities at the LHC and the intrinsic charm in the proton

Rafał Maciuła[1,*] and Antoni Szczurek[1,2,†]

[1]*Institute of Nuclear Physics, Polish Academy of Sciences, ul. Radzikowskiego 152, PL-31-342 Kraków, Poland*

[2]*College of Natural Sciences, Institute of Physics, University of Rzeszów, ul. Pigonia 1, PL-35-310 Rzeszów, Poland*

(Received 4 November 2022; accepted 4 January 2023; published 1 February 2023)

We discuss production of far-forward charm and anticharm quarks, D mesons and antimesons, and neutrinos and antineutrinos from their semileptonic decays in proton-proton collisions at the LHC energies. We include the gluon-gluon fusion $gg \to c\bar{c}$, the intrinsic charm (IC) $gc \to gc$ as well as the recombination $gq \to Dc$ partonic mechanisms. The calculations are performed within the k_T-factorization approach and the hybrid model using different unintegrated parton distribution functions (uPDFs) for gluons from the literature, as well as within the collinear approach. We compare our results to the LHCb data for forward D^0-meson production at $\sqrt{s} = 13$ TeV for different rapidity bins in the interval $2 < y < 4.5$. A good description is achieved for the Martin-Ryskin-Watt (MRW) uPDF. We also show results for the Kutak-Sapeta (KS) gluon uPDF, both in the linear form and including nonlinear effects. The nonlinear effects play a role only at very small transverse momenta of D^0 or $\bar{D}^0$ mesons. The IC and recombination models are negligible at the LHCb kinematics. Both the mechanisms start to be crucial at larger rapidities and dominate over the standard charm production mechanisms. At high energies, there are so far no experiments probing this region. We present uncertainty bands for the both mechanisms. Decreased uncertainty bands will be available soon from fixed-target charm experiments in pA collisions. We present also energy distributions for forward electron, muon, and tau neutrinos to be measured at the LHC by the currently operating FASERν experiment, as well as by future experiments like FASERν2 or FLArE, proposed very recently by the Forward Physics Facility project. Again components of different mechanisms are shown separately. For all kinds of neutrinos (electron, muon, tau), the subleading contributions, i.e., the IC and/or the recombination, dominate over light meson (pion, kaon) and the standard charm production contribution driven by fusion of gluons for neutrino energies $E_\nu \gtrsim 300$ GeV. For electron and muon neutrinos, both the mechanisms lead to similar production rates, and their separation seems rather impossible. On the other hand, for $\nu_\tau + \bar{\nu}_\tau$ neutrino flux, the recombination is further reduced making the measurement of the IC contribution very attractive.

DOI: 10.1103/PhysRevD.107.034002

I. INTRODUCTION

At high energies, a process of midrapidity production of charm quark and antiquarks is dominated by fusion of gluons (pair creation mechanisms) and interactions of gluons with light quarks (flavor excitation mechanisms). This process can be well described at a broad energy range within theoretical models based on either the next-to-leading order (NLO) collinear or the k_T-factorization frameworks (see, e.g., Refs. [1–5]). The forward production of charm is not fully under control. There are some mechanisms that may play a role outside the midrapidity region (forward and backward production) not only at high collision energies. There are potentially two QCD mechanisms that may play a role in this region:

(a) the mechanism of production of charm initiated by intrinsic charm, which can be called knockout of the intrinsic charm and
(b) recombination of charm quarks and antiquarks and light antiquarks and quarks.

Recently we have shown that at lower energies, the mechanisms easily mix, and it is difficult to disentangle them in the backward production of D mesons [6]. Nevertheless, such fixed-target experiments provide some

*rafal.maciula@ifj.edu.pl
†antoni.szczurek@ifj.edu.pl

limitations on the not fully explored mechanisms. The associated uncertainties are not small. The asymmetry in the production of D^0 ($\bar{D}^0$) mesons may soon provide interesting information on the recombination mechanism. Some limitations on the intrinsic charm component were obtained recently based on the IceCube neutrino data [7] (see also Ref. [8]). From such experiments, we get roughly the probability to find intrinsic charm in the nucleon $P_{\rm IC} < 1\%$, which is consistent with the central value of the CT14nnloIC PDF global fit [9], as well as with the recent study of the NNPDF group based on machine learning and a large experimental dataset [10].

In this paper, we will discuss far-forward production of charm at the LHC energies. The forward production of charm quarks is associated with forward production of charmed mesons. Their direct measurement in far-forward directions is challenging. The forward production of mesons leads to forward production of neutrinos coming from their semileptonic decays. So far, such neutrinos cannot be measured at the LHC; however, there are some ongoing projects to improve the situation. Recently, several new detectors were proposed to measure the forward neutrinos (e.g., FASERν, SND@LHC, FASERν2, FLArE), according to the Forward Physics Facility (FPF) proposal [11–13]. Here, we wish to summarize the situation for the collider mode of the LHC. Can such measurements provide new interesting information on the poorly known mechanisms? We will try to answer the question.

In principle, our present study extends predictions for the far-forward neutrino fluxes at the LHC reported recently in Refs. [14–16] by taking into account new mechanisms that have not been considered so far in this context.

II. DETAILS OF THE MODEL CALCULATIONS

In the present study, we take into consideration three different production mechanisms of charm, including:

(a) the standard (and usually considered as a leading) QCD mechanism of gluon-gluon fusion: $g^*g^* \to c\bar{c}$ with off-shell initial state partons, calculated both in the full k_T-factorization approach and in the hybrid model;
(b) the mechanism driven by the intrinsic charm component of proton: $g^*c \to gc$ calculated in the hybrid approach with off-shell initial state gluon and collinear intrinsic charm distribution;
(c) the recombination mechanism: $gq \to Dc$, calculated in the leading-order collinear approach.

Calculations of the three contributions are performed following our previous studies reported in Refs. [6,17–20].

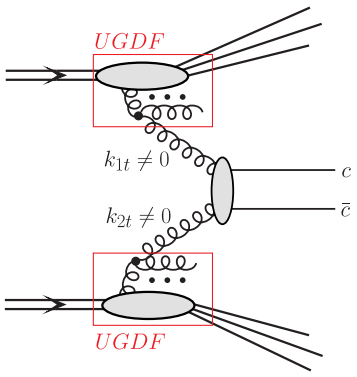

FIG. 1. A diagram of the standard QCD mechanism of charm production in the k_T-factorization approach driven by the fusion of two off-shell gluons.

A. The standard QCD mechanism for charm production

Here, we follow the theoretical formalism for the calculation of the $c\bar{c}$-pair production in the k_T-factorization approach [21]. In this framework, the transverse momenta k_t's (or virtualities) of both partons entering the hard process are taken into account, both in the matrix elements and in the parton distribution functions. Emission of the initial state partons is encoded in the transverse-momentum-dependent (unintegrated) PDFs (uPDFs). In the case of charm flavor production, the parton-level cross section is usually calculated via the $2 \to 2$ leading-order $g^*g^* \to c\bar{c}$ fusion mechanism with off-shell initial state gluons that is the dominant process at high energies (see Fig. 1), especially in the midrapidity region. However, even at extremely backward and forward rapidities, the $q^*\bar{q}^* \to c\bar{c}$ mechanism remains subleading. Then the hadron-level differential cross section for the $c\bar{c}$-pair production, formally at leading order, reads:

$$\frac{d\sigma(pp \to c\bar{c}X)}{dy_1 dy_2 d^2p_{1,t} d^2p_{2,t}} = \int \frac{d^2k_{1,t}}{\pi}\frac{d^2k_{2,t}}{\pi}\frac{1}{16\pi^2(x_1x_2s)^2}\overline{|\mathcal{M}^{\text{off shell}}_{g^*g^*\to c\bar{c}}|^2} \times \delta^2(\vec{k}_{1,t}+\vec{k}_{2,t}-\vec{p}_{1,t}-\vec{p}_{2,t})\mathcal{F}_g(x_1,k_{1,t}^2,\mu_F^2)\mathcal{F}_g(x_2,k_{2,t}^2,\mu_F^2), \tag{2.1}$$

where $\mathcal{F}_g(x_1,k_{1,t}^2,\mu_F^2)$ and $\mathcal{F}_g(x_2,k_{2,t}^2,\mu_F^2)$ are the gluon uPDFs for both colliding hadrons, and $\mathcal{M}^{\text{off shell}}_{g^*g^*\to c\bar{c}}$ is the off-shell matrix element for the hard subprocess. The gluon uPDF depends on gluon longitudinal momentum fraction x, transverse momentum squared k_t^2 of the gluons entering the hard process, and, in general, also on a (factorization) scale of the hard process μ_F^2. They must be evaluated at longitudinal momentum fractions $x_1 = \frac{m_{1,t}}{\sqrt{s}}\exp(y_1) + \frac{m_{2,t}}{\sqrt{s}}\exp(y_2)$, and

$x_2 = \frac{m_{1,t}}{\sqrt{s}}\exp(-y_1) + \frac{m_{2,t}}{\sqrt{s}}\exp(-y_2)$, where $m_{i,t} = \sqrt{p_{i,t}^2 + m_c^2}$ is the quark and antiquark transverse mass.

As we have carefully discussed in Ref. [17], there is a direct relation between a resummation present in uPDFs in the transverse momentum dependent factorization and a parton shower in the collinear framework. In most uPDFs, the off-shell gluon can be produced either from gluon or quark; therefore, in the k_T-factorization, all channels of the higher-order type in the collinear approach driven by gg, $q\bar{q}$ and even by qg initial states are open already at leading order (in contrast to the collinear factorization).

In the numerical calculations below, we apply the Martin-Ryskin-Watt (MRW) [22] gluon uPDFs calculated from the MMHT2014nlo [23] collinear gluon PDF as well as Kutak-Sapeta (KS) [24] linear and nonlinear distributions. As a default set in the numerical calculations, we take the renormalization scale $\mu^2 = \mu_R^2 = \sum_{i=1}^{n} \frac{m_{it}^2}{n}$ (averaged transverse mass of the given final state) and the charm quark mass $m_c = 1.5$ GeV. The strong-coupling constant $\alpha_s(\mu_R^2)$ at next-to-next-to-leading order is taken from the CT14nnloIC PDF [9] routines.

In the parts of the calculations especially devoted to the far-forward production of charm, we also calculate the standard production mechanism with only one gluon being off shell and second one collinear in accordance with the assumptions of the so called hybrid model, which is described in the next subsection.

B. The intrinsic charm induced component

The intrinsic charm contribution to charm production cross section (see Fig. 2) is obtained within the hybrid theoretical model discussed by us in detail in Ref. [19]. The FPF experiments at the LHC will allow us to explore the charm cross section in the far-forward rapidity direction where asymmetric kinematical configurations are selected. Thus, in the basic $gc \to gc$ reaction, the gluon PDF and the intrinsic charm PDF are simultaneously probed at different longitudinal momentum fractions—extremely small for the gluon and very large for the charm quark.

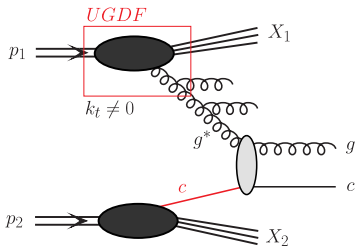

FIG. 2. A diagrammatic representation of the intrinsic charm driven mechanism of charm production within the hybrid model with the off-shell gluon and the on-shell charm quark in the initial state.

Within the asymmetric kinematic configuration $x_1 \ll x_2$, the cross section for the processes under consideration can be calculated in the so-called hybrid factorization model motivated by the work in Ref. [25]. In this framework, the small-x gluon is taken to be off mass shell, and the differential cross section, e.g., for $pp \to gcX$ via $g^*c \to gc$, mechanism reads:

$$d\sigma_{pp\to gcX} = \int d^2k_t \int \frac{dx_1}{x_1} \times \int dx_2 \mathcal{F}_{g^*}(x_1, k_t^2, \mu^2) c(x_2, \mu^2) d\hat{\sigma}_{g^*c\to gc}, \tag{2.2}$$

where $\mathcal{F}_{g^*}(x_1, k_t^2, \mu^2)$ is the unintegrated gluon distribution in one proton and $c(x_2, \mu^2)$ a collinear PDF in the second one. The $d\hat{\sigma}_{g^*c\to gc}$ is the hard partonic cross section obtained from a gauge invariant tree-level off-shell amplitude. A derivation of the hybrid factorization from the dilute limit of the color glass condensate approach can be found, e.g., in Ref. [26] (see also Ref. [27]). The relevant cross sections are calculated with the help of the KATIE Monte Carlo generator [28]. There the initial state quarks (including heavy quarks) can be treated as a massless partons only.

Working with minijets (jets with transverse momentum of the order of a few GeV) requires a phenomenologically motivated regularization of the cross sections. Here, we follow the minijet model [29] adopted, e.g., in the PYTHIA Monte Carlo generator, where a special suppression factor is introduced at the cross section level [30]:

$$F(p_t) = \frac{p_t^2}{p_{T0}^2 + p_t^2}, \tag{2.3}$$

for each of the outgoing massless partons with transverse momentum p_t, where p_{T0} is a free parameter of the form factor that also enters as an argument of the strong coupling constant $\alpha_S(p_{T0}^2 + \mu_R^2)$. A phenomenological motivation behind its application in the k_T-factorization approach is discussed in detail in Ref. [31].

In the numerical calculations below, the intrinsic charm PDFs are taken at the initial scale $m_c = 1.3$ GeV, so the perturbative charm contribution is intentionally not taken into account. We apply different grids of the intrinsic charm distribution from the CT14nnloIC PDF [9] that correspond to the BHPS model [32].

C. Recombination model of charmed meson production

The underlying mechanism of the Braaten-Jia-Mechen (BJM) [33–35] recombination is illustrated in Fig. 3. The differential cross section for production of Dc final state reads:

$$\frac{d\sigma}{dy_1 dy_2 d^2p_t} = \frac{1}{16\pi^2 \hat{s}^2}[x_1 q_1(x_1,\mu^2) x_2 g_2(x_2,\mu^2)\overline{|\mathcal{M}_{qg\to Dc}(s,t,u)|^2} + x_1 g_1(x_1,\mu^2) x_2 q_2(x_2,\mu^2)\overline{|\mathcal{M}_{gq\to Dc}(s,t,u)|^2}]. \tag{2.4}$$

Above, y_1 is rapidity of the D meson and y_2 rapidity of the associated c or $\bar{c}$. The fragmentation of the latter will be discussed below.

The matrix element squared in (2.4) can be written as

$$\overline{|\mathcal{M}_{qg\to Dc}(s,t,u)|^2} = \overline{|\mathcal{M}_{qg\to(\bar{c}q)^n c}|^2}\cdot\rho, \tag{2.5}$$

where n enumerates quantum numbers of the $\bar{c}q$ system $n \equiv {}^{2J+1}L$, and ρ can be interpreted as a probability to form real meson. For illustration, as our default set, we shall take $\rho = 0.1$, but the precise number should be adjusted to experimental data. For the discussion of the parameter, see, e.g., Refs. [34,35] and references therein. The asymmetries observed in photoproduction can be explained with $\rho = 0.15$ [35]. Some constrains for this parameter could be also obtained from the LHCb fixed-target data on D-meson production asymmetry that are going to be published soon [6].

The explicit form of the matrix element squared can be found in [33] for pseudoscalar and vector meson production for color singlet and color octet mesonlike states. Similar formulas can be written for production of $\bar{D}\,\bar{c}$. Then the quark distribution is replaced by the antiquark distribution. In the following, we include only color singlet $(q\bar{c})^n$ or $(\bar{q}c)^n$ components. As a default set, the factorization scale in the calculation is taken as

$$\mu^2 = p_t^2 + \frac{m_{t,D}^2 + m_{t,c}^2}{2}. \tag{2.6}$$

Within the recombination mechanism, we include fragmentation of c quarks or $\bar{c}$ antiquarks accompanying directly produced D mesons or $\bar{D}$ antimesons; e.g.:

$$d\sigma[qg \to \bar{D}_{\text{direct}} + D_{\text{frag}}] = d\sigma[qg \to \bar{D} + c] \otimes F_{c\to D}^{\text{frag}}, \tag{2.7}$$

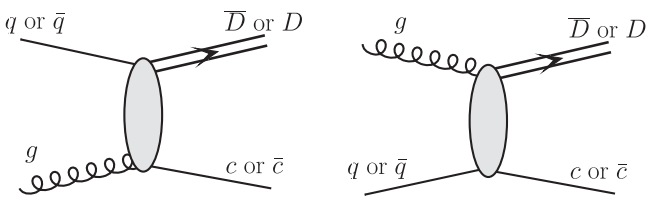

FIG. 3. Generic leading-order diagrams for D-meson production via the BJM recombination.

where $F_{c\to D}^{\text{frag}}$ is the relevant fragmentation function. How the convolution $\otimes$ is understood is explained in [36].

We shall discuss in the present paper also the asymmetry in production of D^0 meson and $\bar{D}^0$ antimeson. The asymmetry is defined as

$$A_p = \frac{d\sigma^{D^0}/d\xi - d\sigma^{\bar{D}^0}/d\xi}{d\sigma^{D^0}/d\xi + d\sigma^{\bar{D}^0}/d\xi}, \tag{2.8}$$

where ξ represents single variable (y or p_t) or even a pair of variables (y, p_t).

Only a part of the pseudoscalar D mesons is directly produced. A second part originates from vector meson decays. The vector D mesons promptly and dominantly decay to pseudoscalar mesons:

$$\begin{aligned} &D^{*0} \to D^0\pi(0.619), D^0\gamma(0.381),\\ &D^{*+} \to D^0\pi^+(0.677), D^+\pi^0(0.307), D^+\gamma(0.0016),\\ &D_s^{*+} \to D_s^+\gamma(0.935), D_s^+\pi^0(0.058), D_s^+e^+e^-(6.710^{-3}). \end{aligned} \tag{2.9}$$

D. Hadronization of charm quarks

The transition of charm quarks to open charm mesons is done in the framework of the independent parton fragmentation picture (see, e.g., Ref. [36]), where the inclusive distributions of open charm meson can be obtained through a convolution of inclusive distributions of produced charm quarks and antiquarks and $c \to D$ fragmentation functions. Here, we follow exactly the method that was applied by us in our previous study of forward and backward charm production reported, e.g., in Ref. [20]. According to this approach, we assume that the D meson is emitted in the direction of parent c quark and antiquark, i.e., $\eta_D = \eta_c$ (the same pseudorapidities or polar angles), and the z-scaling variable is defined with the light-cone momentum; i.e., $p_c^+ = \frac{p_D^+}{z}$ where $p^+ = E + p$. In numerical calculations, we take the Peterson fragmentation function [37] with $\varepsilon = 0.05$, often used in the context of hadronization of heavy flavors. Then, the hadronic cross section is normalized by the relevant charm fragmentation fractions for a given type of D meson [38]. In the numerical calculations below, when discussing D^0-meson production for the $c \to D^0$ transition, we take the fragmentation probability $\mathrm{P}_{c\to D^0} = 61\%$.

TABLE I. Leading decay channels resulting in production of ν_μ and ν_e neutrinos.

Neutrino source	Leading decay channels	BR [%]
Charged pions	$\pi^+ \to \mu^+\nu_\mu$	99.99
Kaons: K^+, K_L	$K^+ \to \mu^+\nu_\mu$	63.56
	$K^+ \to \pi^0\mu^+\nu_\mu$	3.35
	$K^+ \to \pi^0 e^+\nu_e$	5.07
	$K^+ \to e^+\nu_e$	1.58×10^{-5}
	$K_L \to \pi^\pm\mu^\mp\nu_\mu$	27.04
	$K_L \to \pi^\pm e^\mp\nu_e$	40.55
Charm mesons:	$D^+ \to \bar{K}^0\mu^+\nu_\mu$	8.76
D^+, D^0, D_S^+	$D^+ \to K^-\pi^+\mu^+\nu_\mu$	3.65
	$D^+ \to \bar{K}^0 e^+\nu_e$	8.72
	$D^+ \to K^-\pi^+ e^+\nu_e$	4.02
	$D^0 \to K^-\mu^+\nu_\mu$	3.41
	$D^0 \to K^*(892)\mu^+\nu_\mu$	1.89
	$D^0 \to K^- e^+\nu_e$	3.55
	$D^0 \to \bar{K}^0\pi^- e^+\nu_e$	1.44
	$D^0 \to K^*(892) e^+\nu_e$	2.15
	$D^0 \to K^-\pi^0 e^+\nu_e$	1.60
	$D_s^+ \to \eta e^+\nu_e$	2.32
	$D_s^+ \to \eta\mu^+\nu_\mu$	2.40
	$D_s^+ \to \phi e^+\nu_e$	2.39
	$D_s^+ \to \phi\mu^+\nu_\mu$	1.9
	$D_s^+ \to \eta' e^+\nu_e$	8.00×10^{-3}
	$D_s^+ \to \eta'\mu^+\nu_\mu$	1.01
Muons	$\mu^- \to e^-\bar{\nu}_e\nu_\mu$	≈100

E. Production of ν_e and ν_μ neutrinos

There are different sources of neutrinos (see Ref. [39]). In general, the ν_e neutrinos can be produced from the decays of K^+ and K_L mesons and the ν_μ neutrinos from K^+, K_L and π^+. In addition, both of them can be also produced from D^+, D^0, D_S^+ mesons via many decay channels. Another important source of ν_e and ν_μ is also decay of muons. The latter component is important for large distances, $c\tau = 659$ m [39]. The planned neutrino target (the target where neutrinos are measured) will be placed 480 m from the interaction point. This requires more dedicated studies. In addition, there are many sources of muons. Reliable estimation would require evolution of produced neutrinos through the rock between the production point and analyzing target. All the most important decay channels for ν_e and ν_μ neutrinos are collected in Table I.

In the present study, we are particularly interested in D-meson semileptonic decays. As will be discussed below, we have no such decay functions. In practical evaluation, often a simplified decay function for kaon decays [40] is used also to the decays of charm mesons $D \to M_{\rm eff} l^+\nu_l$, where $M_{\rm eff}$ is the effective invariant mass squared in the decay, by replacing $m_K \to m_D$ in the simplified formula:

$$G(x) = \frac{12x^2(1-\epsilon^2-x)^2}{g(\epsilon)(1-x)}, \tag{2.10}$$

where $g(\epsilon) = 1 - 8\epsilon^2 - 24\epsilon^4 \ln\epsilon + 8\epsilon^6 - \epsilon^8$ with $\epsilon = M_{\rm eff}/m_D$, and $x = 2E_\nu^*/m_D$ with kinematical limits $0 \le x \le 1-\epsilon^2$.

By fitting the data in Ref. [41], the authors find: $M_{\rm eff} = 0.63$ GeV for $D^\pm$, and $M_{\rm eff} = 0.67$ GeV for $D^0/\bar{D}^0$—almost the same number for both species of D mesons. Such a form is not completely correct as there are several final channels with a neutrino and antineutrino, as discussed above.

In the future, one could use also more theoretically motivated D-meson decay functions obtained from semileptonic transition form factors (see, e.g., Ref. [42]) or use directly experimental data for semileptonic transition form factor measured last years by the BESIII collaboration [43].

An alternative way to incorporate semileptonic decays into theoretical model is to take relevant experimental input. Here, we follow the method described in Refs. [2,44,45]. For example, the CLEO [46] collaboration has measured very precisely the momentum spectrum of electrons and positrons coming from the decays of D mesons. This is done by producing resonances: $\Psi(3770)$, which decays into D and $\bar{D}$ mesons.

This less ambitious but more pragmatic approach is based on purely empirical fits to (not absolutely normalized) CLEO experimental data points. These electron decay functions should account for the proper branching fractions, which are known experimentally (see, e.g., [39,46]). The branching fractions for various species of D mesons are different:

$$\begin{aligned} {\rm BR}(D^+ \to e^+\nu_e X) &= 16.13 \pm 0.20({\rm stat.}) \pm 0.33({\rm syst.})\%, \\ {\rm BR}(D^0 \to e^+\nu_e X) &= 6.46 \pm 0.17({\rm stat.}) \pm 0.13({\rm syst.})\%. \end{aligned} \tag{2.11}$$

Because the shapes of positron spectra for both decays are identical within error bars, we can take the average value (for $D^\pm$ and D^0) of ${\rm BR}(D \to e\nu_e X) \approx 10\%$ and simplify the calculation.

After renormalizing to experimental branching fractions, the adjusted decay function is then used to generate leptons in the rest frame of the decaying D meson in a Monte Carlo approach. In the case of semileptonic decays of D mesons, relevant for electron and muon neutrinos and antineutrinos, we generate 1000 decays for each considered (generated) D meson. This way, one can avoid all uncertainties associated with explicit calculations of semileptonic decays of mesons.

The open charm mesons are almost at rest, so, in practice, one measures the meson rest frame distributions of electrons and positrons. With this assumption, one can find a good fit to the CLEO data with

$$f_{\rm CLEO}^{\rm Lab}(p) = 12.55(p+0.02)^{2.55}(0.98-p)^{2.75}. \tag{2.12}$$

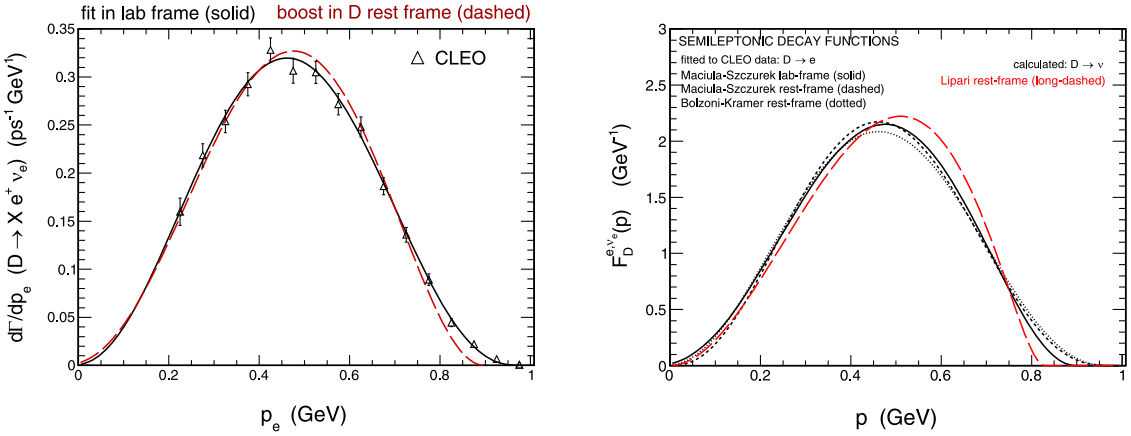

FIG. 4. Left panel: Fits to the CLEO data. The solid lines correspond to the parametrizations in the laboratory frames and the dashed lines to the meson rest frames, which represent incorporation of effects related to the nonzero motion of decaying mesons. Right panel: A comparison of different decay functions normalized to 1 taken from the literature.

In these purely empirical parametrizations, p must be taken in GeV.

In order to take into account the small effect of the nonzero motion of the D mesons in the case of the CLEO experiment, the above parametrization of the fit in the laboratory frame has to be modified. The improvement can be achieved by including the boost of the new modified rest frame functions to the CLEO laboratory frame. The quality of fit from Eq. (2.12) will be reproduced. The D rest frame decay function takes the following form:

$$f^{\mathrm{Rest}}_{\mathrm{CLEO}}(p) = 12.7(p + 0.047)^{2.72}(0.9 - p)^{2.21}. \quad (2.13)$$

Both laboratory and rest frame parametrizations of the semileptonic decay functions for D meson are drawn in the left panel of Fig. 4 together with the CLEO experimental data. Some small differences between the different parametrizations appear only at larger values of electron momentum. The influence of this effect on differential cross sections of leptons is expected to be negligible. As can be seen from the right panel of Fig. 4, our analytical formulas for the decay functions (solid and dashed lines) only slightly differ from the one obtained in a similar approach in Ref. [45] (dotted line) and from the one calculated by using the Lipari's formula [40] (long-dashed formula) described in Eq. (2.10).

The phenomenological model for production of leptons from the semileptonic D-meson decays in hadronic reactions, based on the experimental decay functions described above, has been found to give a very good description of the LHC experimental data collected, e.g., with the ALICE detector [47].

F. Production of ν_τ neutrino

The production mechanism of ν_τ or $\bar{\nu}_\tau$ is a bit more complicated. The decay of D_s mesons to ν_e and ν_μ are often neglected as the relevant $c \to D_s$ fragmentation fraction is relatively small $\mathrm{BR}(c \to D_s) \approx 8\%$, and further decay branching fractions to ν_e and ν_μ are about 2% only. On the other hand, the D_s mesons are also a source of ν_τ neutrinos and antineutrinos. The D_s mesons are quite unique in the production of ν_τ, in particular, decay of D_s mesons is the dominant mechanism of ν_τ production.

In hadronic reactions, such neutrinos and antineutrinos come from the decay of D_s mesons. There are two mechanisms described shortly below:

(a) the direct decay mode: $D_s^+ \to \tau^+\nu_\tau$ with $\mathrm{BR} = 5.32 \pm 0.11\%$ and
(b) the chain decay mode: $D_s^+ \to \tau^+ \to \bar{\nu}_\tau$.

More information can be found in Ref. [48] dedicated to the SHIP fixed-target experiment where the production of the ν_τ neutrinos in a fixed-target $p + {}^{96}\mathrm{Mo}$ reaction at $\sqrt{s} = 27.4$ GeV was discussed. Here, we discuss $p + p$ collisions in their center of mass system, which is also laboratory system for the experimental setup.

1. Direct decay of $D_s^\pm$ mesons

The considered here decay channels: $D_s^+ \to \tau^+\nu_\tau$ and $D_s^- \to \tau^-\bar{\nu}_\tau$, which are the sources of the direct neutrinos, are analogous to the standard text book cases of $\pi^+ \to \mu^+\nu_\mu$ and $\pi^- \to \mu^-\bar{\nu}_\mu$ decays, discussed in detail in the past (see, e.g., Ref. [49]). The same formalism used for the pion decay applies also to the D_s meson decays. Since pion has spin zero, it decays isotropically in its rest frame. However, the produced muons are polarized in its direction of motion, which is due to the structure of weak interaction in the Standard Model. The same is true for $D_s^\pm$ decays and polarization of $\tau^\pm$ leptons.

As it was explicitly shown in Ref. [48], the τ lepton takes almost the whole energy of the mother D_s meson. This is because of the very similar mass of both particles: $m_\tau = 1.777$ GeV and $m_{D_s=1.968}$ GeV. The direct neutrinos

take only a small part of the energy and therefore, will form the low-energy component of the neutrino flux observed by the FASERν experiment.

2. Neutrinos from chain decay of τ leptons

The τ decays are rather complicated due to having many possible decay channels [39]. Nevertheless, all confirmed decays lead to production of ν_τ ($\bar{\nu}_\tau$). This means total amount of neutrinos and antineutrinos produced from D_s decays into the τ lepton is equal to the amount of antineutrinos and neutrinos produced in the subsequent τ decay, but their energy distributions will be different [48].

The purely leptonic channels (three-body decays), analogous to the $\mu^\pm \to e^\pm(\bar{\nu}_\mu/\nu_\mu)(\nu_e/\bar{\nu}_e)$ decay (discussed, e.g., in Refs. [49,50]), cover only about 35% of all τ lepton decays. Remaining 65% are semileptonic decays. They differ quite drastically from each other, and each gives slightly different energy distribution for ν_τ ($\bar{\nu}_\tau$). In our model for the decay of D_s mesons, there is almost full polarization of τ particles with respect to the direction of their motion.

Since $P_{\tau^+} = -P_{\tau^-}$ and the angular distributions of polarized $\tau^\pm$ are antisymmetric with respect to the spin axis, the resulting distributions of ν_τ and $\bar{\nu}_\tau$ from decays of $D_s^\pm$ are then identical, consistent with CP symmetry (see, e.g., Ref. [51]).

In the numerical calculations of ν_τ neutrinos and antineutrinos, we use a sample of 10^5 decays generated before by the dedicated TAUOLA program [52] in the D_s center of mass. The distributions (event by event) are transformed then to the proton-proton center of mass system, which is also a laboratory system where the measurement takes place. Then the momentum and rapidity distributions are obtained, and cuts on (pseudo)rapidity of neutrinos are imposed.

We are interested in energy distribution (fluxes) of different kinds of neutrinos and antineutrinos. In the present paper, we do not simulate interactions of neutrinos with a dedicated target, so we will not estimate actual number of experimental events for FASERν. Such a number would depend on a given target used in the experiment. As discussed in the result section, already the flux of neutrinos and anineutrinos corresponding to different mechanisms will allow to draw very interesting conclusions, especially on the intrinsic charm in the proton.

III. NUMERICAL RESULTS

We start our presentation of results from the forward production of D mesons at the LHC energy $\sqrt{s} = 13$ TeV within the LHCb experiment rapidity acceptance, i.e., $2 < y < 4.5$. In Fig. 5, we show transverse momentum and rapidity distributions of $D^0 + \bar{D}^0$ calculated within the full k_T-factorization approach (solid histograms) as well as within the hybrid model (dotted histograms), for the MRW-MMHT2014nlo gluon uPDFs. Here, and in the following, the on-shell collinear parton distributions are taken from the MMHT2014nlo PDF set [23]. The theoretical predictions are compared to the LHCb experimental data [53]. Here, a very good agreement with the LHCb data is obtained with the full k_T-factorization calculations. The hybrid model seems to underestimate the experimental distributions at more central rapidities; however, both predictions starts to coincide in the more forward region, i.e., $4.5 < y < 6.5$, beyond the LHCb detector coverage. In the far-forward region ($y > 6.5$), the hybrid approach leads to slightly larger cross sections than the full k_T-factorization.

In Fig. 6, we show a similar theory-to-data comparison as above, but here, we plot numerical results obtained with the KS linear (solid histograms) and nonlinear (dotted histograms) gluon uPDFs. Both calculations here are obtained within the hybrid approach. The KS uPDFs are available only for $x < 10^{-2}$, so they cannot be used on the large-x side in the full k_T-factorization calculations, especially in the case of forward charm production. As we can see, the difference between predictions of the linear and nonlinear uPDFs appear only at very small transverse

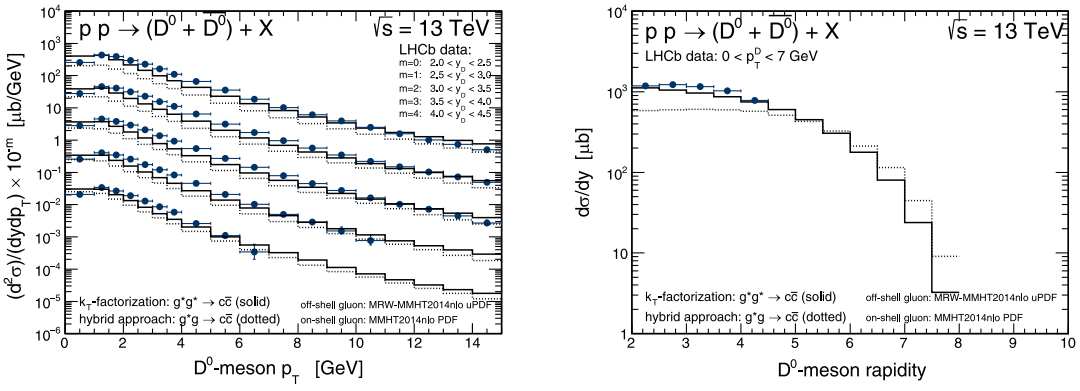

FIG. 5. Transverse momentum distributions for different windows of rapidity (left panel) and rapidity distribution (right panel) of $D^0 + \bar{D}^0$ mesons at $\sqrt{s} = 13$ TeV, obtained with the MRW-MMHT2014nlo gluon uPDF together with the LHCb data [53]. Details are specified in the figure.

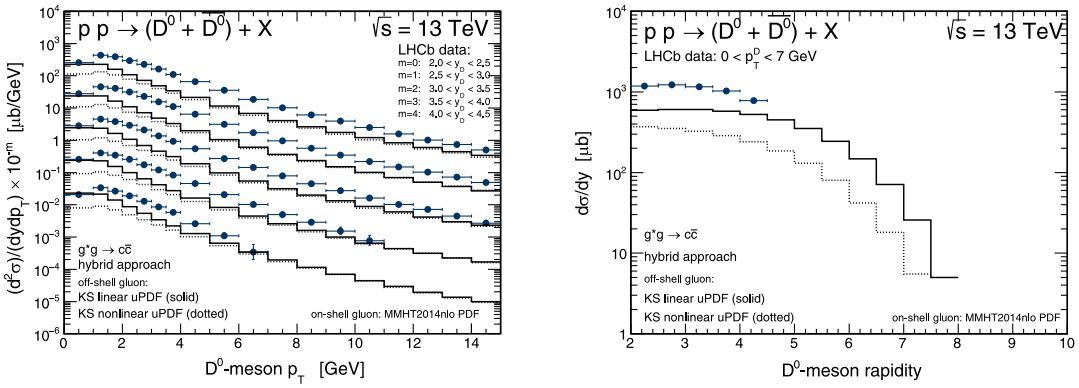

FIG. 6. Transverse momentum distributions for different windows of rapidity (left panel) and rapidity distribution (right panel) of $D^0 + \bar{D}^0$ mesons at $\sqrt{s} = 13$ TeV, obtained in the hybrid approach with the KS linear and KS nonlinear gluon uPDFs together with the LHCb data [53]. Details are specified in the figure.

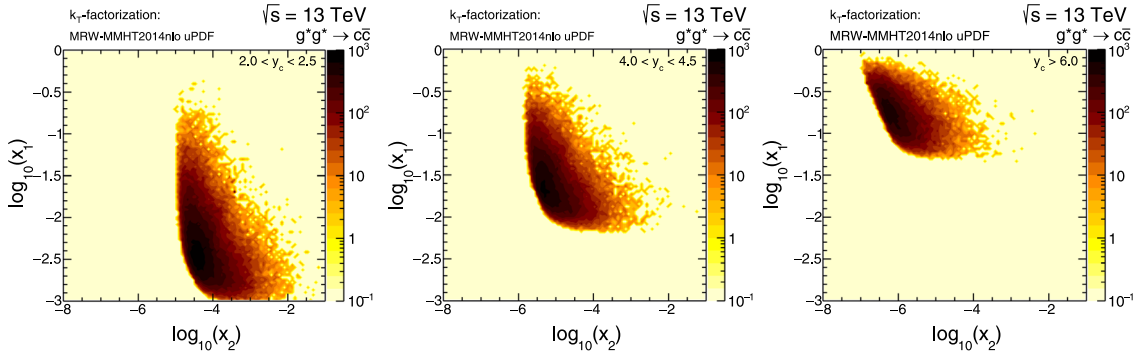

FIG. 7. Two-dimensional distribution in $\log_{10}(x_1)$ and $\log_{10}(x_2)$ for different windows of rapidity calculated in the full k_T-factorization approach for the MRW-MMHT2014nlo uPDF.

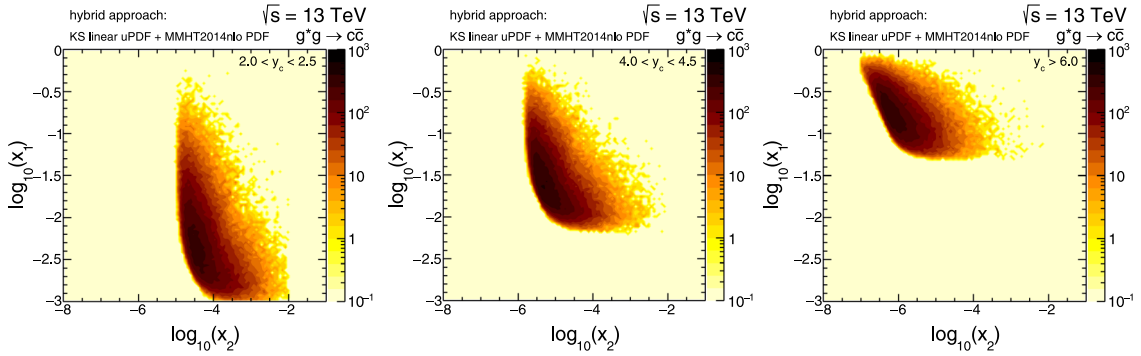

FIG. 8. Two-dimensional distribution in $\log_{10}(x_1)$ and $\log_{10}(x_2)$ for different windows of rapidity calculated in the hybrid model for the KS linear uPDF.

momenta. Unfortunately, both of them visibly underestimate the LHCb data points; however, the discrepancy seems to decrease when moving to more forward rapidities. Therefore, one should not discard them in the far-forward limit.

In Figs. 7 and 8, we show the region of longitudinal momentum fractions of gluons entering the fusion process for different windows of rapidity. We observe that even in the current LHCb acceptance, one deals with the very asymmetric configurations where $x_1 \gg x_2$. The situation

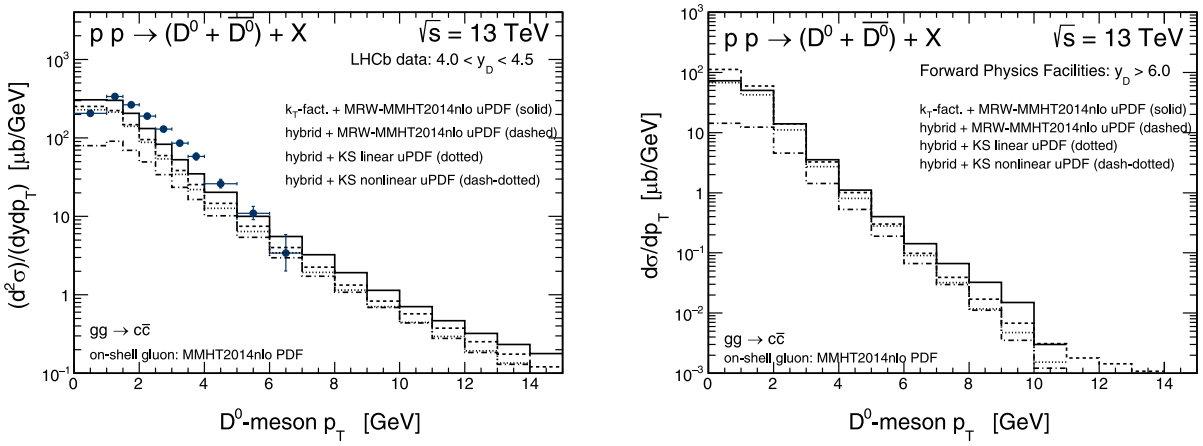

FIG. 9. Transverse momentum distribution of $D^0 + \bar{D}^0$ mesons for $4.0 < y < 4.5$ (left panel) and $y > 6$ (right panel) for $\sqrt{s} = 13$ TeV. We show result for the k_t-factorization as well as for the hybrid approach.

depends on the rapidity interval, and for most forward LHCb interval of rapidity, one probes x_2 down to $\approx 10^{-5}$, (a typical region where one could expect the onset of saturation effects) and simultaneously x_1 above 10^{-2}. The kinematical configuration becomes even more interesting and challenging when approaching the far-forward region, taking, e.g., $y > 6.0$, where one could probe $x_1 > 0.1$ and $x_2 < 10^{-6}$.

Let us concentrate now on the most forward D meson production. In the left panel of Fig. 9, we show result for the most forward LHCb rapidity bin ($4 < y < 4.5$) obtained within the k_T-factorization approach as well as results for the hybrid approach. The hybrid approach for the MRW-MMHT2014nlo and the KS linear uPDF (dashed and dotted lines, respectively) gives an only somewhat smaller cross section than the k_T-factorization approach for the MRW-MMHT2014nlo uPDF (solid lines). Only the hybrid predictions for the KS nonlinear uPDF (dash-dotted lines) seems to be completely disfavored by the LHCb data.

In the right panel, we show similar results but for $y > 6$, not accessible so far at the LHC for the D meson production. Here, the prediction of the full k_T-factorization for the MRW-MMHT2014nlo uPDF coincides with those calculated with the hybrid model for the MRW-MMHT2014nlo and the KS linear uPDF. The three different calculations lead to very similar results in the far-forward limit of charm production, which leaves a slight freedom of their choice.

So far, we have considered only the dominant at midrapidity gluon-gluon fusion mechanism of charm production. Now, we shall consider the subdominant at midrapidities the intrinsic charm and the recombination contributions. The free parameters $P_{\rm IC}$ for the intrinsic charm and ρ for the recombination mechanisms used in this

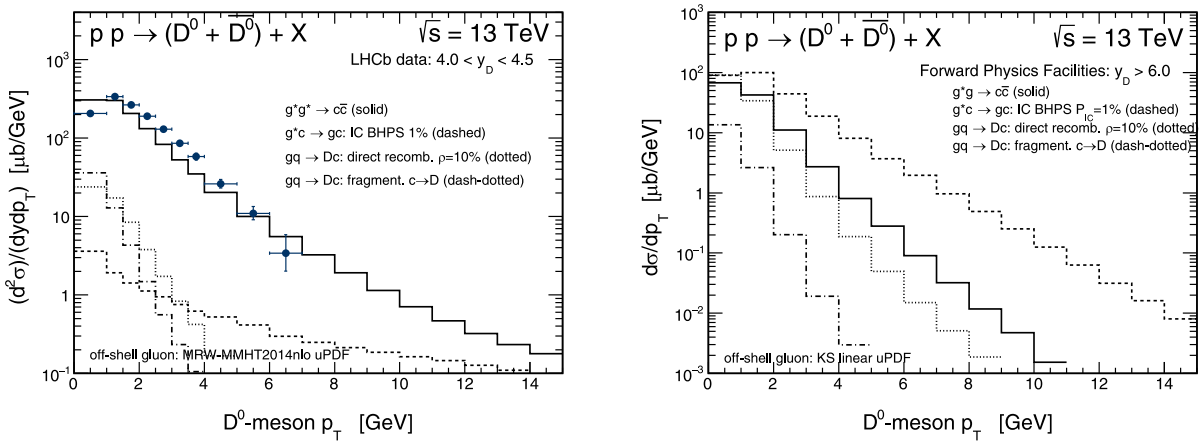

FIG. 10. Transverse momentum distributions of $D^0 + \bar{D}^0$ for the most forward LHCb rapidity bin (left panel) and for $y > 6$ (right panel) for $\sqrt{s} = 13$ TeV. We show separately the gg-fusion (solid), the intrinsic charm (dashed), and the two contributions of recombination (dotted and dash-dotted) mechanisms.

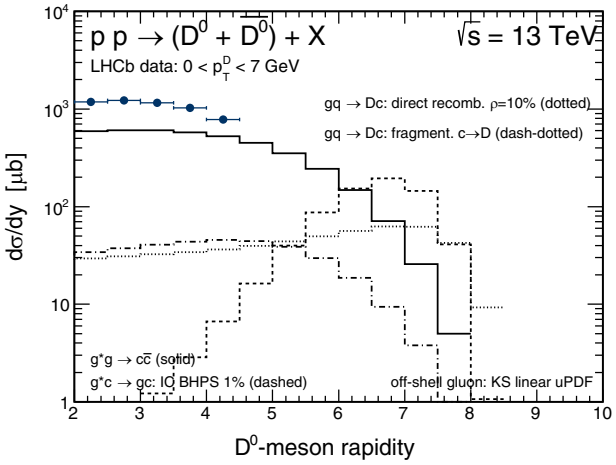

FIG. 11. Rapidity distribution of $D^0 + \bar{D}^0$ for $\sqrt{s} = 13$ TeV. We show separately the gg-fusion (solid), the intrinsic charm (dashed), and the two contributions of recombination (dotted and dash-dotted) mechanisms.

calculation are those found in our recent analyses of the high-energy neutrino IceCube data [7] and of the fixed-target LHCb charm data [6]. In Fig. 10, we show transverse momentum distributions for the most forward measured rapidity bin of the LHCb collaboration (left panel) and for $y > 6$ (right panel). The contributions of the subleading mechanisms in the region measured by the LHCb seem completely negligible. The situation changes dramatically for larger rapidities. There, the intrinsic charm contribution (dashed lines) becomes larger than and the recombination contribution (dotted and dash-dotted lines) is of a similar size as the well-known standard gg-fusion component calculated here in the hybrid model (solid lines).

The rapidity distribution of $D^0 + \bar{D}^0$, shown in Fig. 11, nicely summarizes the situation. Both the IC and the recombination contributions have a distinct maximum at $y \sim 7$, where they dominate over the standard mechanism. In the far-forward region, the IC contribution is larger than the recombination and the standard components

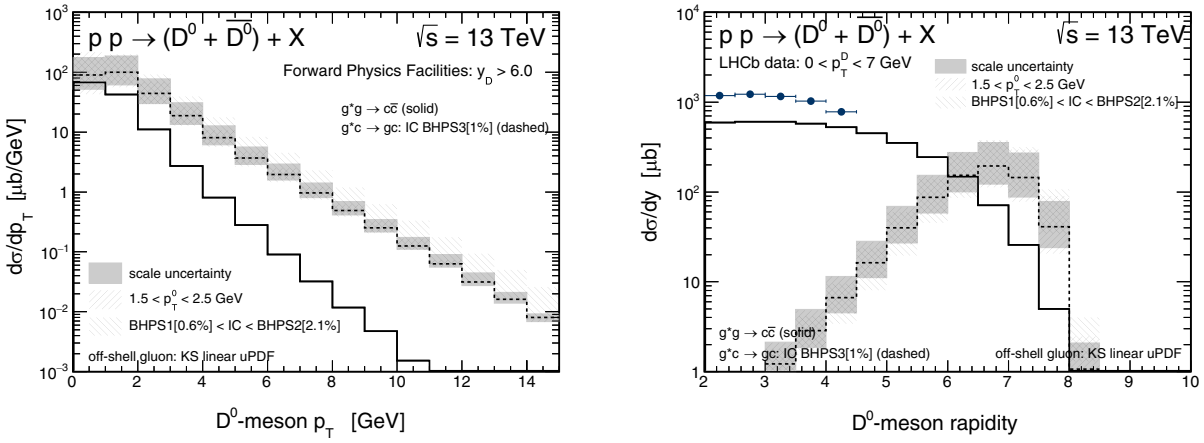

FIG. 12. The scale, P_{IC} and p_{T0} uncertainty bands for the IC contribution.

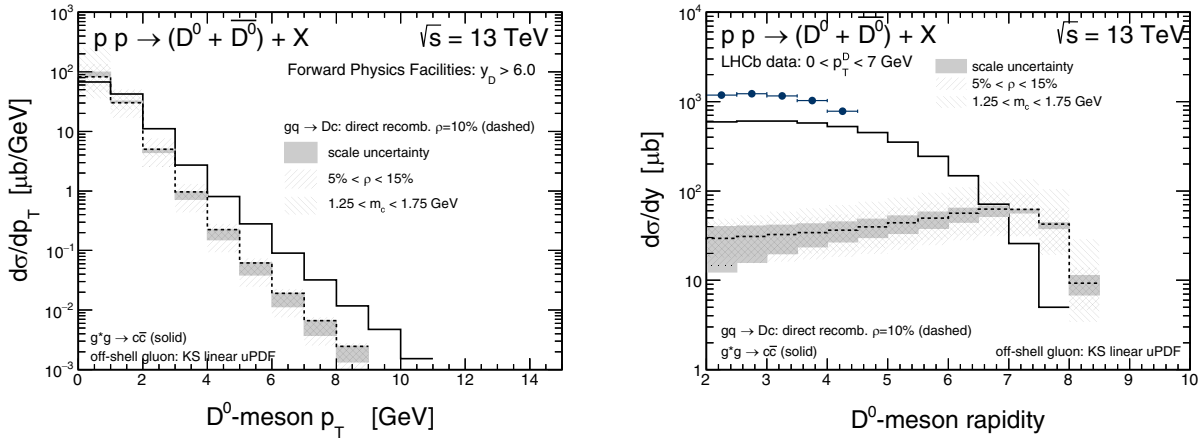

FIG. 13. The scale, ρ and m_c uncertainty bands for the direct recombination contribution.

approximately by a factor of 3 and 6, respectively. The relative contribution of the IC to the forward charm cross section could be even larger if a cut on the low meson transverse momenta is imposed.

The uncertainties of the calculations of the standard charm production mechanism have been discussed many times in our previous studies (see, e.g., Ref. [1]) and will be not repeated here. How uncertain are the IC and the recombination contributions is shown in Figs. 12 and 13, respectively. In the case of the intrinsic charm mechanism, we plot uncertainties related to the scales, the p_{T0} parameter, as well as due to the $P_{\rm IC}$ probability in the BHPS model. In the case of the recombination component, we show uncertainties related to the scales, charm quark mass, and the recombination probability ρ. The uncertainties are quite sizeable; however, even when taking the lower limits of the IC and the recombination predictions, one could expect a visible enhancement of the forward charm cross section with respect to the standard calculations. The scenario with upper limits can be examined by the future FPF LHC data.

Now we proceed to neutrino and antineutrino production. In Fig. 14, we show energy distribution of $\nu_e + \bar{\nu}_e$ calculated for the $\sqrt{s} = 13$ TeV, including the designed psuedorapidity acceptance $\eta > 8.5$ of the FASERν experiment. Here, and in the following, the number of neutrinos is obtained for the integrated luminosity $L_{\rm int} = 150$ fb^{-1}. In addition to the production from the semileptonic decays of D mesons, we show contribution from the decay of kaons (dotted line) taken from [15]. The gluon-gluon fusion contribution is quite small, visibly smaller than the kaon contribution. Both the IC and recombination contributions may be seen as an enhancement over the contribution due to conventional kaons in the neutrino energy distribution at neutrino energies $E_\nu > 1$ TeV; however, size of the effect is rather small. An identification of the subleading contributions will require a detailed comparison to the

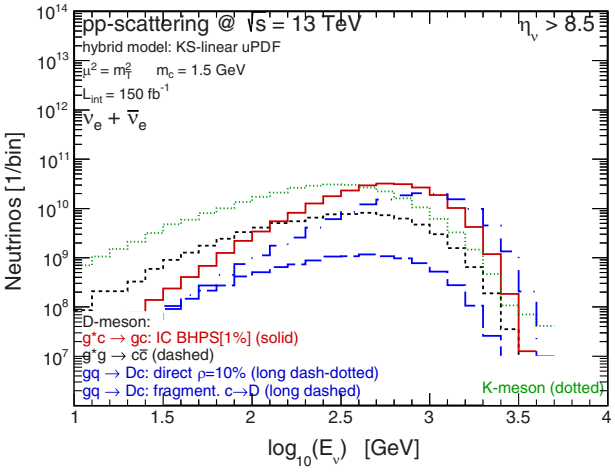

FIG. 14. Energy distribution of electron neutrinos + anineutrinos for $\eta > 8.5$ (FASERν).

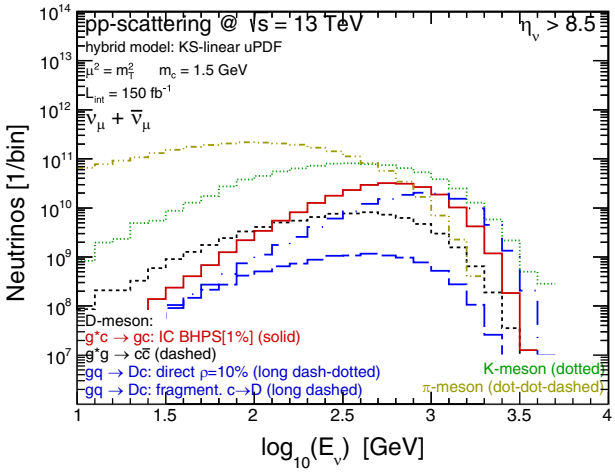

FIG. 15. Energy distribution of muon neutrinos + anineutrinos for $\eta > 8.5$ (FASERν).

FASERν data. Here, the recombination and IC contributions may be of a similar order.

The situation for muon neutrinos is much more difficult as here a large conventional contribution from charged pion decays enters [15]. As it is shown in Fig. 15, here the IC and recombination contributions are covered by the $\pi \to \nu_\mu$ (dot-dot-dashed), $K \to \nu_\mu$ (dotted) contributions even at large neutrino energies.

Another option to identify the subleading contributions is to investigate energy distributions of ν_τ neutrinos which are, however, difficult to measure experimentally. Such distributions are shown in Fig. 16. Here again, the contribution of subleading mechanisms dominates over the traditional gluon-gluon fusion mechanism. In addition, there is no contribution of light mesons due to limited phase space for τ production in the D_s decay. In this case, the contribution due to recombination is small compared to electron and muon neutrinos case because $s(x) \ll u_{\rm val}(x), d_{\rm val}(x)$.

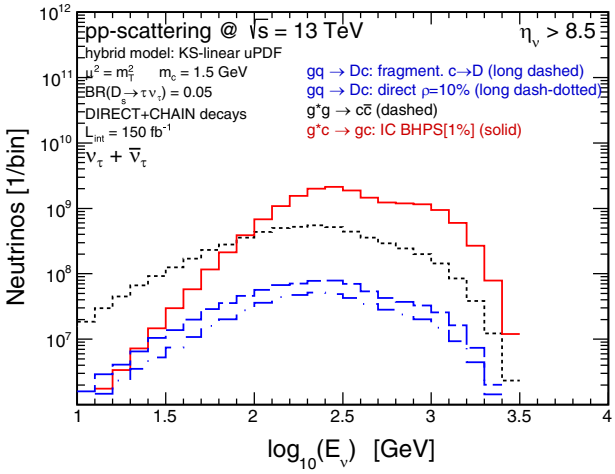

FIG. 16. Energy distribution of tau neutrinos + anineutrinos for $\eta > 8.5$ (FASERν).

Therefore, the measurement of ν_τ and/or $\bar{\nu}_\tau$ seems optimal to pin down the IC contribution in the nucleon.

IV. CONCLUSIONS

In this paper, we have discussed forward production of charm quarks, charmed mesons, and different types of neutrinos at the LHC energies. Different mechanisms have been considered. The gluon-gluon fusion production of charm has been calculated within the k_T-factorization and hybrid approaches with different unintegrated gluon distributions from the literature.

We have calculated transverse momentum distributions of $D^0 + \bar{D}^0$ for different bins of meson rapidities. The results of the calculations have been compared to the LHCb experimental data. A very good agreement has be achieved for the Martin-Ryskin-Watt unintegrated gluon distribution for each bin of rapidity. The Kutak-Sapeta model gives a somewhat worse description of the LHCb data. Both models lead, however, to similar predictions for far-forward charm production.

We have discussed the range of gluon longitudinal momentum fractions for different ranges of rapidity. Already, the LHC data test longitudinal gluon momentum fractions as small as 10^{-5}.

We have shown that the intrinsic charm and recombination contributions give a rather negligible contribution for the LHCb rapidity range. However, in very forward directions, the mechanisms start to be crucial. Using estimation of model parameters obtained recently from the analysis of fixed-target data, we have presented our predictions for the LHC energy $\sqrt{s} = 13$ TeV. Both the considered "subleading" mechanisms win in forward directions with the dominant at midrapidity gluon-gluon fusion component. However, it is not possible to verify the prediction for the D mesons experimentally.

We have calculated also different species of neutrinos and antineutrinos from semileptonic decays of different species of D mesons. There is a good chance that energy distributions of ν_e neutrinos may provide some estimation on the subleading IC and recombination mechanisms. However, the two subleading mechanisms compete. The energy spectrum of ν_τ neutrinos coming from the decay of D_s mesons may provide valuable information on the size of the intrinsic charm since here the recombination mechanism is reduced due to the smallness of strange quark distributions. In addition, in this case, there are no conventional contributions related to semileptonic decays of pions and kaons.

In summary, we think that the measurement of energy distributions of far-forward neutrinos and antineutrinos should provide new information on subleading contributions to charm production, especially on the intrinsic charm content of the proton. Very large fluxes of high-energy neutrinos for FASERν have been predicted. A realistic simulation of the target for neutrino measurement should be performed in future.

ACKNOWLEDGMENTS

This study was supported by the Polish National Science Center Grant No. UMO-2018/31/B/ST2/03537 and by the Center for Innovation and Transfer of Natural Sciences and Engineering Knowledge in Rzeszów.

[1] R. Maciuła and A. Szczurek, Phys. Rev. D **87**, 094022 (2013).
[2] R. Maciuła, A. Szczurek, and M. Łuszczak, Phys. Rev. D **92**, 054006 (2015).
[3] M. Cacciari, S. Frixione, N. Houdeau, M. L. Mangano, P. Nason, and G. Ridolfi, J. High Energy Phys. 10 (2012) 137.
[4] B. A. Kniehl, G. Kramer, I. Schienbein, and H. Spiesberger, Eur. Phys. J. C **72**, 2082 (2012).
[5] M. Klasen, C. Klein-Bösing, K. Kovarik, G. Kramer, M. Topp, and J. Wessels, J. High Energy Phys. 08 (2014) 109.
[6] R. Maciula and A. Szczurek, Phys. Lett. B **835**, 137530 (2022).
[7] V. P. Goncalves, R. Maciula, and A. Szczurek, Eur. Phys. J. C **82**, 236 (2022).
[8] R. Laha and S. J. Brodsky, Phys. Rev. D **96**, 123002 (2017).
[9] T. J. Hou, S. Dulat, J. Gao, M. Guzzi, J. Huston, P. Nadolsky, C. Schmidt, J. Winter, K. Xie, and C. P. Yuan, J. High Energy Phys. 02 (2018) 059.
[10] R. D. Ball, A. Candido, J. Cruz-Martinez, S. Forte, T. Giani, F. Hekhorn, K. Kudashkin, G. Magni, and J. Rojo *et al.* (NNPDF Collaboration), Nature (London) **608**, 483 (2022).
[11] H. Abreu *et al.* (FASER Collaboration), Eur. Phys. J. C **80**, 61 (2020).
[12] SND and LHC Collaborations, arXiv:2210.02784.
[13] L. A. Anchordoqui, A. Ariga, T. Ariga, W. Bai, K. Balazs, B. Batell, J. Boyd, J. Bramante, M. Campanelli, A. Carmona *et al.*, Phys. Rep. **968**, 1 (2022).
[14] W. Bai, M. Diwan, M. V. Garzelli, Y. S. Jeong, and M. H. Reno, J. High Energy Phys. 06 (2020) 032.
[15] F. Kling and L. J. Nevay, Phys. Rev. D **104**, 113008 (2021).
[16] W. Bai, M. Diwan, M. V. Garzelli, Y. S. Jeong, F. K. Kumar, and M. H. Reno, J. High Energy Phys. 06 (2022) 148.
[17] R. Maciula and A. Szczurek, Phys. Rev. D **100**, 054001 (2019).
[18] R. Maciuła, Phys. Rev. D **102**, 014028 (2020).
[19] R. Maciuła and A. Szczurek, J. High Energy Phys. 10 (2020) 135.

[20] R. Maciula and A. Szczurek, Phys. Rev. D **105**, 014001 (2022).
[21] S. Catani, M. Ciafaloni, and F. Hautmann, Phys. Lett. B **242**, 97 (1990); Nucl. Phys. **B366**, 135 (1991); Phys. Lett. B **307**, 147 (1993); J. C. Collins and R. K. Ellis, Nucl. Phys. **B360**, 3 (1991).L. V. Gribov, E. M. Levin, and M. G. Ryskin, Phys. Rep. **100**, 1 (1983); E. M. Levin, M. G. Ryskin, Yu. M. Shabelsky, and A. G. Shuvaev, Sov. J. Nucl. Phys. **53**, 657 (1991).
[22] G. Watt, A. D. Martin, and M. G. Ryskin, Eur. Phys. J. C **31**, 73 (2003).
[23] L. A. Harland-Lang, A. D. Martin, P. Motylinski, and R. S. Thorne, Eur. Phys. J. C **75**, 204 (2015).
[24] K. Kutak, Phys. Rev. D **91**, 034021 (2015).
[25] M. Deak, F. Hautmann, H. Jung, and K. Kutak, J. High Energy Phys. 09 (2009) 121.
[26] A. Dumitru, A. Hayashigaki, and J. Jalilian-Marian, Nucl. Phys. **A765**, 464 (2006).
[27] P. Kotko, K. Kutak, C. Marquet, E. Petreska, S. Sapeta, and A. van Hameren, J. High Energy Phys. 09 (2015) 106.
[28] A. van Hameren, Comput. Phys. Commun. **224**, 371 (2018).
[29] T. Sjostrand and M. van Zijl, Phys. Rev. D **36**, 2019 (1987).
[30] T. Sjöstrand, S. Ask, J. R. Christiansen, R. Corke, N. Desai, P. Ilten, S. Mrenna, S. Prestel, C. O. Rasmussen, and P. Z. Skands, Comput. Phys. Commun. **191**, 159 (2015).
[31] P. Kotko, A. M. Stasto, and M. Strikman, Phys. Rev. D **95**, 054009 (2017).
[32] S. J. Brodsky, P. Hoyer, C. Peterson, and N. Sakai, Phys. Lett. **93B**, 451 (1980).
[33] E. Braaten, Y. Jia, and T. Mehen, Phys. Rev. D **66**, 034003 (2002).
[34] E. Braaten, Y. Jia, and T. Mehen, Phys. Rev. Lett. **89**, 122002 (2002).
[35] E. Braaten, Y. Jia, and T. Mehen, Phys. Rev. D **66**, 014003 (2002).
[36] R. Maciuła and A. Szczurek, J. Phys. G **47**, 035001 (2020).
[37] C. Peterson, D. Schlatter, I. Schmitt, and P. M. Zerwas, Phys. Rev. D **27**, 105 (1983).
[38] M. Lisovyi, A. Verbytskyi, and O. Zenaiev, Eur. Phys. J. C **76**, 397 (2016).
[39] R. L. Workman *et al.* (Particle Data Group), Prog. Theor. Exp. Phys. **2022**, 083C01 (2022).
[40] P. Lipari, Astropart. Phys. **1**, 195 (1993).
[41] E. V. Bugaev, A. Misaki, V. A. Naumov, T. S. Sinegovskaya, S. I. Sinegovsky, and N. Takahashi, Phys. Rev. D **58**, 054001 (1998).
[42] Z. Q. Yao, D. Binosi, Z. F. Cui, C. D. Roberts, S. S. Xu, and H. S. Zong, Phys. Rev. D **102**, 014007 (2020).
[43] Y. H. Yang (BESIII Collaboration), arXiv:1812.00320.
[44] M. Luszczak, R. Maciula, and A. Szczurek, Phys. Rev. D **79**, 034009 (2009).
[45] P. Bolzoni and G. Kramer, Nucl. Phys. **B872**, 253 (2013); **B876**, 334(E) (2013).
[46] N. E. Adam *et al.* (CLEO Collaboration), Phys. Rev. Lett. **97**, 251801 (2006).
[47] B. B. Abelev *et al.* (ALICE Collaboration), Phys. Rev. D **91**, 012001 (2015).
[48] R. Maciuła, A. Szczurek, J. Zaremba, and I. Babiarz, J. High Energy Phys. 01 (2020) 116.
[49] P. Renton, *Electroweak Interactions: An Introduction to the Physics of Quarks and Leptons* (Cambridge University Press, Cambridge, United Kingdom, 1990), 596.
[50] T. K. Gaisser, *Cosmic Rays and Particle Physics* (Cambridge University Press, Cambridge, United Kingdom, 1990), p. 279.
[51] S. M. Barr, T. K. Gaisser, P. Lipari, and S. Tilav, Phys. Lett. B **214**, 147 (1988).
[52] S. Jadach, J. H. Kuhn, and Z. Wąs, Comput. Phys. Commun. **64**, 275 (1990).M. Jeżabek, Z. Wąs, S. Jadach, and J. H. Kuhn, Comput. Phys. Commun. **70**, 69 (1992).S. Jadach, Z. Wąs, R. Decker, and J. H. Kuhn, Comput. Phys. Commun. **76**, 361 (1993).M. Chrzaszcz, T. Przedziński, Z. Wąs, and J. Zaremba, Comput. Phys. Commun. **232**, 220 (2018).
[53] R. Aaij *et al.* (LHCb Collaboration), J. High Energy Phys. 03 (2016) 159; 09 (2016) 013(E); 05 (2017) 074(E).